

Stability of extended defects on boron nitride and graphene monolayers: the role of chemical environment

L. C. Gomes, S. S. Alexandre, H. Chacham, and R. W. Nunes*

Departamento de Física, Universidade Federal de Minas Gerais,

CP 702, 30123-970, Belo Horizonte, MG, Brazil

(Dated: March 21, 2022)

We perform *ab initio* calculations that indicate that the relative stability of antiphase boundaries (APB) with armchair and zigzag chiralities in monolayer boron nitride (BN) is determined by the chemical potentials of the boron and nitrogen species in the synthesis process. In an N-rich environment, a zigzag APB with N-rich core is the most stable structure, while under B-rich or intrinsic growth conditions, an armchair APB with stoichiometric core is the most stable. This stability transition is shown to arise from a competition between homopolar-bond (B-B and N-N) and elastic energy costs in the core of the APBs. Moreover, in the presence of a carbon source we find that a carbon-doped zigzag APB becomes the most stable boundary near the N-rich limit. The electronic structure of the two types of APBs in BN is shown to be particularly distinct, with the zigzag APB depicting defect-like deep electronic bands in the band gap, while the armchair APB shows bulk-like shallow electronic bands.

PACS numbers: 73.22.-f, 73.20.Hb, 71.55.-i

Many proposed applications of nanomaterials require the ability to control their electronic properties. In particular, graphene and boron nitride (BN) in the two-dimensional (2D) monolayer form have become an important subject of research, owing to their mechanical strength and a rich variety of physical phenomena connected to their electronic structure.¹ The introduction of structural defects presents an alternative for manipulating the electronic and magnetic properties in these materials.¹⁻⁷ In graphene grown on Ni(111) substrates, a translational grain boundary (GB) has been theoretically proposed³ and recently observed in STM experiments,⁴ and the occurrence of magnetism for the quasi-one-dimensional electronic states introduced by this defect has been suggested by *ab initio* calculations.⁵ This GB in graphene lies along the zigzag direction and arises due to the presence of two possible stackings of the graphene monolayer with respect to the Ni(111) substrate, which leads to the possibility of domains related by a relative translation, with the GB emerging as the boundary between two such domains.⁴ In the case of monolayer BN grown on Ni(111), the same stacking mechanism holds,⁸ and the possibility of engineering smaller band gaps in this large-band-gap material by the introduction of this zigzag-direction boundary has been recently considered.⁶

In this work, we introduce a low-energy stoichiometric model for an armchair-direction antiphase boundary (APB) in monolayer BN,⁹ based on a structural pattern recently observed experimentally in irradiated graphene.¹⁰ Furthermore, we investigate the electronic properties and compare the stability of several different models for extended one-dimensional (1D) defects in monolayer BN and graphene, including the aforementioned zigzag and armchair boundaries.

Our *ab initio* calculations indicate that in graphene the zigzag GB is more stable than the armchair GB, while in BN the relative stability of APBs with zigzag and arm-

chair chiralities depends on the chemical potentials of the B and N species in the synthesis process, with nitrogen-rich zigzag APBs becoming more stable than stoichiometric armchair APBs only when defects are formed under nitrogen-rich conditions. Moreover, in the presence of carbon dopants, a C-doped zigzag APB becomes the most stable boundary for the last one-third of the interval of realistic B and N chemical potentials values, comprising the last part of the intrinsic region plus the N-rich region. Furthermore, we find that in graphene the armchair GB introduces weaker resonances near the Fermi level (FL), associated to defect states that are only partially confined to the defect core, in contrast with the strongly localized states characteristic of the zigzag GB.⁵ In the case of BN, we find that the armchair APB introduces flat bands near the bulk band edges which are weakly confined to the defect core, while the B-rich, the N-rich, and the C-doped zigzag APBs lead to the formation of electronic bands that are deep in the bulk band gap and strongly localized on the atoms at the defect core.

In graphene, the translational GB observed in Ref. 4 is obtained by cutting a graphene sheet along the zigzag direction, displacing the two halves by one-third of the lattice period in the direction perpendicular to the cut, and inserting carbon dimers with their common bond oriented along the cut, generating a line of pentagon-pentagon-octagon units, as shown in Fig. 1(a). Being oriented along the zigzag direction, this boundary is labeled Z-GB in our discussion.

In the present study, we examine the armchair-direction counterpart of the Z-GB in graphene. The armchair grain boundary, which we label A-GB, can be obtained by cutting a graphene sheet in the armchair direction and translating one side of the sheet with respect to the other side by half the lattice period along the armchair direction, generating a line defect that contains

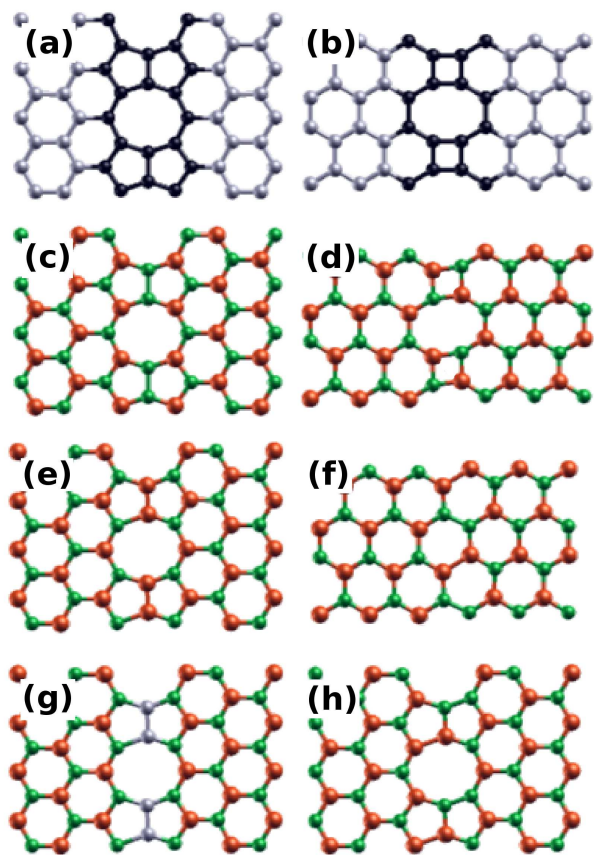


FIG. 1: Structures of grain boundaries (GB) and antiphase boundaries (APB) in monolayer graphene and boron nitride. Boron, nitrogen, and carbon atoms are shown by orange, green, and grey circles, respectively. (a) Z-GB: a graphene GB with zigzag chirality. (b) A-GB: a graphene GB with armchair chirality. (c) NZ-APB: a zigzag APB in BN with N-rich core. (d) A-APB: an armchair APB in BN with stoichiometric core. (e) BZ-APB: a zigzag APB in BN with B-rich core. (f) HA-APB: an armchair APB in BN with stoichiometric core consisting of hexagons with homopolar bonds. (g) CZ-APB: a zigzag APB in BN with carbon-doped core. (h) Z-GB: a zigzag GB in BN with stoichiometric core. Core atoms for zigzag and armchair defects are shown by darker circles in (a) and (b), respectively.

squares and octagons alternately arranged in its core, as shown in Fig. 1(b). Small finite segments of this core structure have been observed in graphene as result of reconstruction after electronic-beam irradiation.¹⁰ Chiral GB geometries may also be built by combining these two basic structures.

In a binary system like monolayer BN, inversion symmetry is absent and an APB is formed at the interface of two domains with opposite assignments of B and N atoms to the two triangular sublattices of the BN honeycomb lattice. In this material, the geometries of the graphene Z-GB and A-GB translate into APBs: the core of the armchair boundary, which we label A-APB, is naturally stoichiometric (having the same number of N and

B atoms) as shown in Fig. 1(d), while for the zigzag APB the core is either N-rich or B-rich, if one adopts the criterion of minimizing the number of homopolar (N-N or B-B) bonds. In our discussion, the N-rich version of the zigzag boundary, shown in Fig. 1(c), is labeled NZ-APB; the boron-rich one, shown in Fig. 1(e), is labeled BZ-APB; a carbon-doped version obtained by replacing the B₂ dimers at the center of the BZ-APB core with C₂ dimers, shown in Fig. 1(g), is labeled CZ-APB. A model for a stoichiometric Z-GB in BN (not an APB in this case) is also possible, at the cost of introducing an extra homopolar bond per defect unit, as shown in Fig. 1(h). We also consider a stoichiometric APB interface in BN containing homopolar bonds without topological defects, shown in Fig. 1(f).

In our study, we employ a first principles approach based on Kohn-Sham density functional theory (KS-DFT),¹¹ as implemented in the SIESTA code.¹² All calculations are performed using the generalized-gradient approximation (GGA) for the exchange-correlation term.¹³ Interactions between valence electrons and ionic cores are described by Troullier-Martins pseudopotentials.¹⁴ A double- ζ pseudoatomic basis set augmented with polarization orbitals is employed, with an energy cutoff of 0.01 Ry. Structural optimization is performed until the residual force on each atom is less than 0.04 eV/Å. Supercells in our study are periodic in the monolayer plane and large vacuum regions are included to impose periodic boundary conditions in the perpendicular direction. Ribbon geometries are described below. Convergence tests were performed and supercell sizes were chosen such that interactions between defects in the plane and between each layer and its periodic images were negligible.

We seek to compare the relative stability of the above 1D defects in graphene and BN. In the case of graphene, the formation energy of the GBs per unit length E_f^{GB} is given by

$$E_f^{GB} = \frac{E_{tot}^{GB}(N) - N\mu_{graph}^{bulk}}{\ell} \quad (1)$$

where $E_{tot}^{def}(N)$ is the total energy of the N -atom supercell containing a GB, $\mu_{graph}^{bulk} = -154.532$ eV is the bulk chemical potential of graphene, obtained as the total energy per atom in a pristine graphene calculation, and ℓ is the length of the supercell along the defect direction.

Our calculated values for E_f^{Z-GB} and E_f^{A-GB} in graphene are included in Table I. In this material, the Z-GB is more stable than the A-GB by 0.25 eV/Å due to the smaller bond-length and bond-angle distortions from the ideal bulk values ($d_{bulk} = 1.442$ Å and $\theta_{bulk} = 120^\circ$ in our calculations) incurred in the pentagon-pentagon-octagon core of the Z-GB, when compared with the tetragon-octagon core of the A-GB. Average bond lengths and bond angles, as well as maximum and minimum values and standard deviations for these quantities are included in Table I for the Z-GB and the A-GB. While average values are similar for both bond

lengths and bond angles, deviations from the bulk reference values are larger in the A-GB core.

This indicates that the nature of the energy difference between the A-GB and the Z-GB in graphene is essentially elastic. Indeed, a Keating-model calculation with a Keating potential fitted for diamond carbon¹⁵ predicts the elastic energy of the A-GB to be about twice that of the Z-GB, in qualitative agreement with our *ab initio* results. A more quantitative agreement would require fitting the Keating potential to the graphene bonding environment.

	E_f	\bar{d}	d_{max}	d_{min}	σ_d	$\bar{\theta}$	θ_{max}	θ_{min}	σ_θ
Z-GB	0.48	1.45	1.48	1.41	0.02	120°	141.7°	104.6°	11.1°
A-GB	0.73	1.44	1.52	1.40	0.04	120°	147.9°	90°	16.8°

TABLE I: Formation energies (E_f in eV/Å), and average, maximum, minimum, and dispersion values for bond lengths (d in Å) and bond angles (θ) for zigzag and armchair grain boundaries in graphene.

In BN, the lack of inversion symmetry means that in a periodic supercell calculation for non-stoichiometric boundaries, such as the NZ-APB and its BZ-APB partner, both boundaries are included in the periodic cell, hence only the sum of the formation energies of the two 1D defects can be extracted from such calculation. Obtaining formation energies of individual boundaries requires using BN ribbons, containing a single boundary in the middle and hydrogen-saturated edges. The ribbons are finite in the direction perpendicular to the 1D boundary and periodic in the parallel direction. Figure 2(a) shows the BN ribbons employed for the NZ-APB calculation, and Fig. 2(b) shows the ribbon employed in the A-APB calculations. The ribbon employed for BZ-APB calculations (not shown in Fig. 2) is obtained from the NZ-APB one by swapping the B and N atoms.

Stoichiometry is determinant for the stability of the various APBs and GBs in BN, since the chemical potentials of the B and N species will depend on the growth conditions, i.e., on the sources of B and N atoms in the synthesis process. The formation energy of the BN ribbons depends on the ribbon stoichiometry and is thus a function of the chemical potentials for B, N, and H. Assuming that defect formation occurs in equilibrium with a bulk BN monolayer, we impose that $\mu_B + \mu_N = \mu_{BN}$, where μ_{BN} is the total energy per BN pair for a pristine BN monolayer, and explore the APB formation energy E_f^{APB} as a function of μ_B and μ_N by defining two limiting chemical potential environments: in the B-rich case μ_B is obtained from the total energy per atom for the α -boron bulk phase ($\alpha - B$), and in the N-rich situation μ_N is obtained from the total energy per atom of an N_2

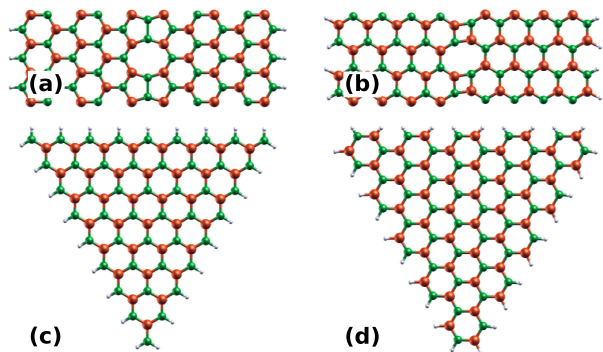


FIG. 2: Ribbon and triangle geometries for computation of extended-defect energies in monolayer boron nitride. (a) Ribbon with N-rich zigzag antiphase boundary in the middle and N-rich zigzag edges. (b) Ribbon with armchair boundary in the middle and armchair edges. (c) Triangle with the same N-rich zigzag edges as ribbon in (a). (d) Triangle with the same armchair edges as ribbon in (b).

molecular crystal calculation. We write

$$\begin{aligned} \mu_N + \mu_B &= \mu_{BN} = -350.187 \text{ eV} ; \\ \mu_N^{max} &= \frac{E_{tot}^{N_2}}{2} = -270.290 \text{ eV} \quad (\text{N-rich}) ; \\ \mu_N^{min} &= \mu_{BN} - \frac{E_{tot}^{\alpha B}}{12} = -273.712 \text{ eV} \quad (\text{B-rich}) . \end{aligned} \quad (2)$$

We emphasize that our range of values for μ_B and μ_N are determined for a condition of equilibrium with solid-state phases of BN and N (or B). These physical constraints, previously considered in calculations of defects in bulk BN,¹⁶ BCN monolayers,¹⁷ BN fullerenes,^{18,19} and BN nanocones,²⁰ have not been considered in a recent calculation.²¹ As shown in the following, the determination of physically acceptable ranges for μ_N and μ_B is crucial to determine which extended defect structure is the most stable under N-rich, intrinsic, or B-rich conditions.

Given the chemical potentials in Eq. 2, we define the formation energy of the BN ribbons E_f^{rib} , which includes the formation energies of the APB and of the edges, as follows:

$$\begin{aligned} E_f^{rib} &= \frac{E_{tot}^{rib} - N_B \mu_B - N_N \mu_N - N_H \mu_H}{\ell} \\ E_f^{rib} &= E_f^{APB} + 2E_f^{edge} . \end{aligned} \quad (3)$$

where E_{tot}^{rib} is the calculated total energy of the ribbon, ℓ is the length of the ribbon along the APB direction, N_B , N_N , and N_H are the numbers of boron, nitrogen, and hydrogen atoms in the ribbon, and μ_B , μ_N , and μ_H are the respective chemical potentials.

In order to obtain E_f^{APB} from Eq. 4 above, we follow the procedure from Ref. 21 and consider BN triangles in which the three hydrogen-saturated edges are the same as those in the corresponding ribbons, as shown in Fig. 2. The formation energy of an N -atom triangle E_f^Δ is defined similarly to Eq. 3, and can be decomposed into

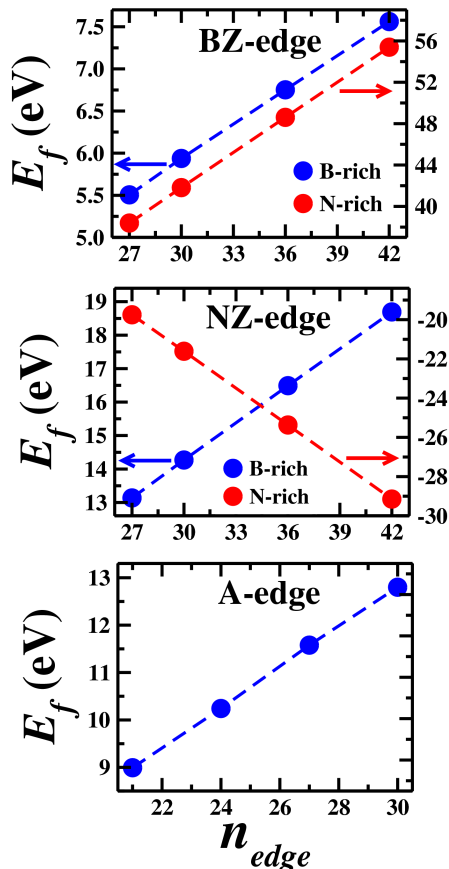


FIG. 3: Formation energy of BN triangles as a function of the number of edge units. The upper (middle) panel shows the energies of the NZ-edge (BZ-edge) for N-rich and B-rich environments. The lower panel shows the energy of the stoichiometric A-edge.

three components: a bulk one that scales with the area of the triangle ($\propto N$), an edge one that scales with the edge length ($\propto N^{1/2}$), and a vertex component that does not scale with the size of the triangle. Since the bulk of the triangles is composed of BN units, and BN bulk is our reference chemical potential (c.f. Eqs. 2 and 3), the bulk component of E_f^Δ vanishes by definition. It is then possible to obtain the edge energy per edge unit, by considering triangles of different sizes, and fitting E_f^Δ to a linear form:

$$E_f^\Delta = \lambda_f^{edge} n_{edge} + E_f^{vtx}; \quad (5)$$

where λ_f^{edge} is the edge energy per edge unit, n_{edge} is the number of edge units in the triangle, which for zigzag-edge triangles and ribbons is the number of N (B) atoms saturated with one hydrogen in Fig. 2, and for armchair-edge triangles and ribbons is the number of boat-like BN units at the edges. E_f^{vtx} is the contribution from the three vertices of the triangles.

The fittings we obtain for the energies of the triangles shown in Fig. 2(c), with N-rich zigzag edges (NZ-edge),

and for the triangles with B-rich zigzag edges (BZ-edge), under B-rich and N-rich environments, are shown in the upper and middle panels of Fig. 3, respectively. From the slope of the curves in Fig. 3 we obtain the NZ-edge and BZ-edge energies included in Table II. In order to check the consistency of our approach, we also compute the edge energy for triangles shown in Fig. 2(d) with armchair edges (A-edge), and E_f^{A-APB} from Eq. 4 for the ribbon containing an A-APB and armchair edges, shown in Fig. 2(b). The fitting of the energies of the armchair-edge triangles is shown in the lower panel in Fig. 3, and the energy of the A-edge is also included in Table II. The A-edge is stoichiometric, hence its energy is independent of the B and N chemical potentials.

	λ_f^{edge} (eV)		E_f^{vtx} (eV)	
A-edge	0.43		0.06	
	B-rich	N-rich	B-rich	N-rich
NZ-edge	0.37	-0.59	3.15	-2.56
BZ-edge	0.14	1.09	1.83	7.54

TABLE II: Edge energy per edge unit λ_{form}^{edge} and vertex energy E_f^{vtx} , obtained from fitting of triangle energies to Eq. 5, for the armchair edge (A-edge), the N-rich zigzag edge (NZ-edge), and the B-rich zigzag edge (BZ-edge).

It is worth commenting on the negative slope of E_f for the NZ-edge under an N-rich environment. It indicates that the reaction by which hydrogen saturates the edge is exothermic and is consistent with experimental observations of a very high stability for nitrogen-terminated edges in BN islands.²²⁻²⁴ Indeed, the strong tendency of BN patches to display a triangular shape is connected with the stability of the NZ-edges.

Having obtained E_f^{edge} from the above procedure, we can obtain E_f^{APB} from Eq. 4. The results for the five APB models, as well as E_f^{Z-GB} for the Z-GB in BN, as functions of μ_N , are shown in Fig. 4. For the stoichiometric models E_f^{APB} is independent of μ_N . The consistency of the above procedure is attested by the fact that E_f^{APB} values obtained using supercells and the H-terminated ribbons agree to within 0.6% in all cases, as included in Table III (for the NZ-APB NZ-APB we compare the sum of the formation energies).

It is evident that the A-APB is the more stable undoped boundary across $\sim 80\%$ of the range of chemical potentials we consider, with the NZ-APB becoming the most stable one in the N-rich limit of μ_N . In the presence of a carbon source, the carbon-doped CZ-APB is the least stable in a B-rich environment, but becomes the most stable boundary for about one third of the interval of μ_N values, from the end of the intrinsic regime through the N-rich limit. We note that the elastic-energy cost of the A-APB should be even higher than that for the A-GB in graphene, because in BN the bond angles at the core of the defect depart even more strongly from the ideal bulk value of 120° than in graphene, as can

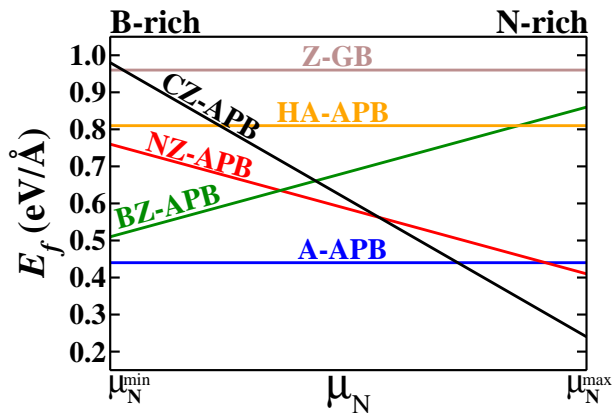


FIG. 4: Formation energy E_f of grain boundaries and antiphase boundaries in boron nitride as a function of the nitrogen chemical potential μ_N . The maximum and minimum values of μ_N are given in the text (see Eq. 2)

be seen in Fig 1. Unlike the case in graphene, however, BN strongly prefers even-membered topological defects in order to avoid the energetically expensive homopolar bonds, except in the N-rich limit where N-N bonds become more favorable.¹⁸

Boundary	E_f (eV/Å)	
	supercell	ribbon
A-APB	0.44	0.44
HA-APB	0.81	0.81
Z-GB	0.96	0.95
NZ-APB + BZ-APB	1.27	1.27
	N-rich - ribbon	B-rich - ribbon
NZ-APB	0.41	0.76
BZ-APB	0.86	0.51
CZ-APB	0.19	0.98

TABLE III: Comparison of formation energy values E_f of grain boundaries and antiphase boundaries in monolayer BN computed with supercells and ribbon geometries. Supercells are stoichiometric and corresponding E_f values do not depend on chemical potentials of B and N. For the ribbons, values for N-rich and B-rich environments are included.

We can use a combination of two models to understand qualitatively the ordering of E_f values in Fig. 4. The idea is to divide the contributions to the formation energies of the boundaries in two components, an elastic one E_{el} , which we estimate by employing a Keating potential fitted for cubic BN,²⁵ and a chemical energy E_Q that is computed using the bond-energy model developed in Ref. 17 to account for the energetics of CBN sheets of various stoichiometries. In this latter model, two-atom bonds are assigned bond-energy values, which reflect the average energy of each type of bond across the various BCN sheets included in the fitting procedure.

The bond-energy values derived in Ref. 17 are $\varepsilon_{CC} = -103.24$ eV, $\varepsilon_{BN} = -116.73$ eV, $\varepsilon_{CN} = -141.67$ eV,

$\varepsilon_{BB} = -50.40$ eV, and $\varepsilon_{NN} = -178.49$ eV, for carbon-carbon, boron-nitrogen, carbon-nitrogen, boron-boron, and nitrogen-nitrogen bonds, respectively. Within the model, the values of E_Q for one period of either the H-APB or the Z-GB, as well as the sum of E_Q values for one period of the NZ-APB and the BZ-APB, should all be ~ 4.62 eV higher than the value for the A-APB, i.e., $E_Q^{H-APB} = E_Q^{Z-GB} = E_Q^{(NZ+BZ)-APB} = E_Q^{A-APB} + 4.62$ eV. Using the BN Keating potential from Ref. 25, we compute the values of E_{el} for the five different boundaries. Results for E_{el} , E_Q , and $E_f = E_Q + E_{el}$ for the A-APB, H-APB, Z-GB, and the sum of the values for the NZ-APB and BZ-APB, computed using this scheme, are included in Table IV.

Boundary	E_Q (eV/Å)	E_{el} (eV/Å)	E_f (eV/Å)
A-APB	0.00	1.02	1.02
NZ-APB + BZ-APB	0.92	1.08	2.00
HA-APB	1.06	0.18	1.24
Z-GB	0.93	0.70	1.63

TABLE IV: Formation energy of grain boundaries and antiphase boundaries in monolayer BN from combination of elastic energy and chemical-bond energy models.

Despite the fact that this simplified partition of E_f fails in describing, even qualitatively, the energy difference between the A-APB and the average of the NZ-APB and BZ-APB, it correctly predicts that the Z-GB has the highest value of E_f , followed by the H-APB. This modeling is useful because it allows us to establish that E_Q is the predominant factor in determining the relative stability of the various boundary models in our study. Note the very low value of E_{el} for the H-APB, with a defect core consisting of hexagons only, which is offset by the high energy cost of two “wrong” bonds per defect unit in the core. On the other hand, the highest value of E_{el} is found for the A-APB, being associated with the strong departure from the bulk bond lengths and bond angles in the fourfold and eightfold rings at the core of this boundary. However, this is compensated by the fact that the chemical energy cost for the A-APB is very low ($E_Q^{A-APB} = 0$ within the simplified bond-energy model above).

Again, a quantitative agreement between the above modeling and the *ab initio* results would require fitting both the Keating potential and the bond-energy model to bonding environments that are more similar to those in the boundary geometries in our study. This analysis also provides a qualitative explanation for one of the ingredients that determines the stability of the carbon-doped CZ-APB boundary: because this structure is obtained from the BZ-APB by replacing the B₂ dimer in the center of the defect core with a C₂ dimer, the elastic energy is reduced because the length of the C-C bonds is similar to the length of the BN bulk matrix, unlike the longer B₂-dimer bond. The other ingredient is electronic, and

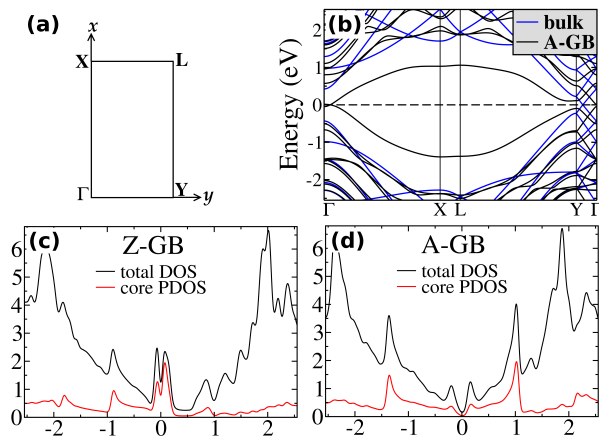


FIG. 5: Band structure and density of states for the A-GB and Z-GB in graphene. (a) Brillouin zone corresponding to the supercell calculations in the present study. (b) Black curves show the A-GB supercell band structure. Blue curves show bulk bands folded onto defect supercell. (c) and (d) show total density of states (DOS) and the DOS projected on the core atoms for the Z-GB and A-GB, respectively.

is determined by stoichiometry (i.e., the chemical potentials) and the fact that in low coordination bonding environments a B-B bond is strongly less favorable than a C-C bond.

Let us now examine the electronic structure of the graphene boundaries. The electronic structure of the Z-GB in graphene has been discussed in Ref. 5, where the appearance of a highly-localized quasi-1D state, introduced by this boundary in the density of states (DOS) of graphene, has been shown to lead to a magnetic instability. [The Z-GB is labeled $\text{GB}(2,0)|(2,0)$ in the notation employed in Ref. 5.] Figures 5(b) and (d) show the electronic band structure and the DOS for the A-GB in graphene, and the DOS for the Z-GB is shown in Fig. 5(c) for comparison. The Brillouin zone corresponding to all defect supercells in this work is shown in Fig. 5 (a). The Γ -X and Y-L lines are parallel to the defect direction (the x -axis of the supercell) in all cases. In order to identify the boundary-related electronic bands, and also to examine the degree of localization of the corresponding states on the core of the boundaries, we project the DOS onto the orbitals centered on the core atoms in each case. The core atoms for each defect geometry are shown by darker circles in Fig. 1(a) and (b), and we use the same definition of defect core for the graphene and BN boundaries.

From the A-GB band structure, we can see that this boundary introduces only small electron and hole pockets near the Fermi level (FL), that show as two weak resonances within ± 0.2 eV from the FL in the DOS. The degree of localization of these electronic states on the eight atoms located at the A-GB core is much weaker than what is found for the magnetic resonance in the Z-GB case.⁵ In the latter case, nearly 90% of the DOS

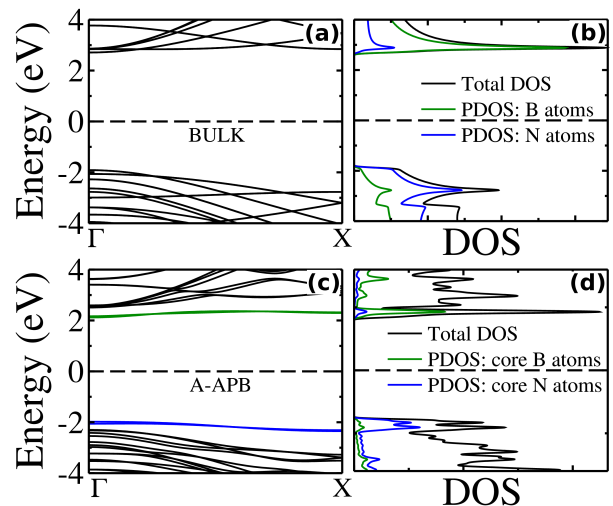


FIG. 6: (a) and (b) Band structure and density of states for bulk BN. Blue and green curves in (b) show the contributions of orbitals of the N and B atoms to the total DOS, respectively. (c) and (d) Band structure and density of states for the A-APB in BN. The contribution of the core-atom orbitals to the total DOS is shown by blue (N orbitals) and green (B orbitals) curves in (d). Defect bands in the gap are shown by green and blue curves, according to the dominant atomic-orbital contribution in each case.

derives from the ten core atoms. This is shown by the partial DOS (PDOS) for the core atoms as red curves in Fig. 5(b) and (d). In the A-GB case, these resonances are much more spread out into the bulk of the cell, and the contribution from the core atoms is much smaller than in the Z-GB. The A-GB also gives rise to stronger resonances at ± 1.0 eV from the FL, connected to the flat portion of the defect bands seen in the band structure in Fig. 5(a)].

In the case of BN, we concentrate on the low-energy A-APB, NZ-APB, BZ-APB, and CZ-APB models. In Fig. 6(a) and (b) we show the band structure and the density of states (DOS) for a pristine bulk BN monolayer. For ease of comparison, the bulk calculation was performed for a supercell of nearly the same dimensions as those employed for the BN boundaries. For our discussion, the important features of the bulk electronic structure are the size of the gap (~ 4.7 eV within the GGA-DFT scheme) and the composition of the electronic states at the band edges: the top of the valence band is mainly composed of nitrogen p_z orbitals while the bottom of the conduction band derives from the boron p_z orbitals.

The electronic bands and the corresponding DOS for the A-APB are shown in Fig. 6(c) and (d). The A-APB introduces one set of two bands near each of the band edges, that show little dispersion and retain the character of the corresponding parent bulk bands. The acceptor bands near the valence-band maximum (VBM) are composed primarily of nitrogen p_z orbitals, while the donor bands near the conduction-band minimum (CBM) con-

sist of boron p_z orbitals, with $\sim 40\%$ of the DOS concentrated on the core atoms in both cases, as shown by the core-projected PDOS curve in Fig. 6. Both sets of bands are shallow (~ 0.2 eV split from the corresponding band edges), and the lack of sizeable dispersion indicates very large effective masses and low mobilities of carriers, should doping of A-GB defect bands become feasible.

The NZ-APB and BZ-APB display much richer electronic structures. The bands and DOS curves for these boundaries are shown in Fig. 7. We include in this figure the electronic states of the boundaries obtained from the ribbon calculations, from which we can identify the states from each of the boundaries individually. One observation regarding the consistency of this procedure is that the electronic states associated with the edges of the ribbon are either shallow or resonant with the bulk bands, and do not mix with the defect bands, as can be observed in the PDOS plots in Fig. 7(b) and (d) for the NZ-APB and the BZ-APB, respectively. This allows us to easily identify the gap states associated with the NZ-APB and BZ-APB. Moreover, we verify that the electronic structure we obtain from the supercell calculation [not shown in Fig. 7 for conciseness], which contains the states from both boundaries, is very consistent with a superposition of the corresponding states from the ribbons for each boundary, in the range of energies of the defect gap states shown in this figure.

Generally, we can see in Fig. 7 that the NZ-APB and BZ-APB boundaries introduce much deeper defect bands into the gap of the BN bulk, resulting in a much larger reduction of the electronic band gap in the spatial region surrounding either the NZ-APB or the BZ-APB⁶ than in the case of the A-APB. Furthermore, the dispersions for these bands are much larger, indicating carrier with potentially larger mobilities than in the A-GB states.

The electronic structure of the BZ-APB ribbon is shown in Fig. 7(a) and (b). Because boron-boron bonds tend to be much longer than the other bonds in these BN systems, the BZ-APB introduces a large compressive strain in its neighborhood, and we observe three defect bands connected with this boundary. Starting from the lower part of the gap, we observe a shallower band with an extended van Hove singularity connected to a large flat portion of this band, starting at the Γ point and extending up to the k-point at ~ 0.6 of the Γ -X line, after which it disperses down and mixes with the bulk states, when reaching the X point at the edge of the one-dimensional BZ. This band derives primarily from the orbitals of the N atoms located on the BN zigzag chains in the core of the BZ-APB ($\sim 58\%$ of the total DOS), with smaller contributions from the zigzag B atoms ($\sim 8\%$), and from the two atoms forming the B_2 dimer at the geometric center of the defect ($\sim 3\%$).

The BZ-APB also introduces a deeper flat band lying ~ 0.5 eV above the VBM, with a total dispersion of ~ 0.2 eV. This band is very strongly localized on the B_2 dimer at the center, with $\sim 75\%$ of the total DOS deriving from the orbitals of the dimer atoms, with smaller contribu-

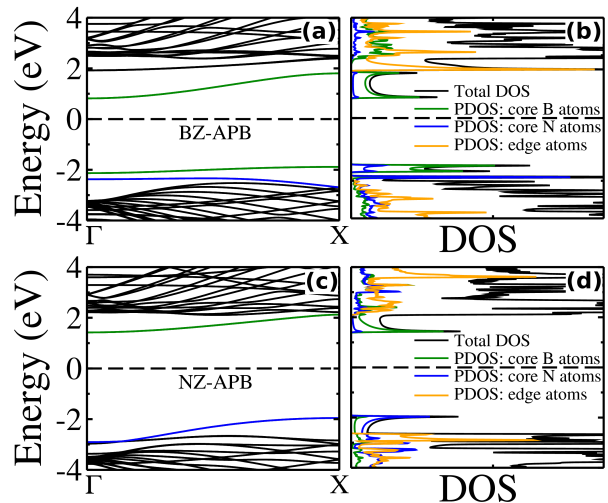


FIG. 7: Band structure along the Γ -X line (parallel to the APB direction) and density of states: (a) and (b) for the BZ-APB; and (c) and (d) for the NZ-APB. The contribution of the core-atom orbitals to the total DOS is shown by blue (N orbitals) and green (B orbitals) PDOS curves in (b) and (d). Defect bands in the gap are shown by green and blue curves, according to the dominant atomic-orbital contribution in each case. The DOS features associated to the ribbon-edge states are shown by orange curves in (b) and (d).

tions of $\sim 12\%$ and $\sim 4\%$ from the N and B atoms on the BN zigzag chains in the core, respectively. The characteristic 1D van Hove singularities associated with the minimum and maximum of this band can be observed in the DOS plot in Fig. 7(b).

In the upper part of the gap, the BZ-APB introduces a deep dispersive band that lies ~ 1.7 eV below the CBM, at the Γ point, and at the X point it reaches its maximum of ~ 0.7 eV below the CBM, for a total dispersion of 1 eV. This band is composed mostly of orbitals of the B atoms at the BZ-APB core, with 53% of the DOS coming from the B_2 dimer at the center and 25% from the B atoms on the BN zigzag chains shouldering the B_2 dimer. A smaller contribution of 8% derives from the N core atoms on the zigzag chains.

Electronic bands, DOS, and PDOS for the NZ-APB ribbon are shown in Fig. 7(c) and (d). In the lower part of the gap this boundary introduces a band with a maximum energy of ~ 0.7 eV above the VBM, near the edge of the BZ at the X point, that shows a dispersion of ~ 1.0 eV. Its minimum is at the Γ point where it becomes resonant and mixed with the bulk states in the VBM region. For most of the Γ -X line of the 1D BZ this band is deep in the gap and strongly localized, with $\sim 88\%$ of the DOS concentrated on the NZ-APB core atoms ($\sim 73\%$ on the N core atoms). In the DOS plot, this bands shows a 1D van Hove singularity above the peak corresponding to the VBM.

In the upper part of gap, the NZ-APB also introduces a band near the CBM that shows similar characteristics as

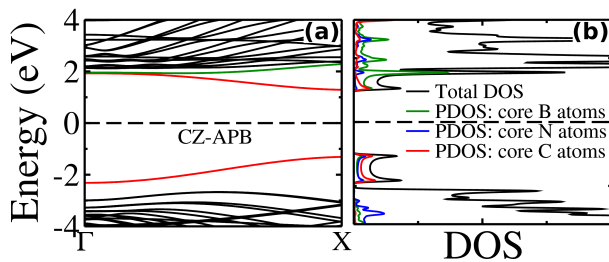


FIG. 8: Band structure along the Γ -X line (parallel to the APB direction) and density of states for the CZ-APB. In (b) the contribution of the core-atom orbitals to the total DOS is shown by blue (N orbitals), green (B orbitals), and red (C orbitals) PDOS curves. Defect bands in the gap are shown by green and red curves, according to the dominant atomic-orbital contribution in each case.

the above one, being deep in the gap near Γ and becoming shallow and mixed with the bulk states when it reaches the edge of the BZ at the X point. This band is very strongly localized on the B and N atoms along the zigzag chain in the core of the NZ-APB, with $\sim 84\%$ of the DOS concentrated on the orbitals of the B atoms and $\sim 7\%$ on the orbitals of the N atoms. The corresponding 1D van Hove singularity is seen in the DOS plot in Fig. 7(d).

The electronic states of the CZ-APB show a similar pattern. We observe the appearance of two bands that are reminiscent of those of a one-dimensional dimerized chain of carbon atoms, with a gap of ~ 2.6 eV at the BZ edge, and dispersions of ~ 1.0 eV (0.6 eV) for the lower (higher) band. The higher band is derived equally from C and B orbitals, while the lower band is dominated by the C orbitals, but with sizeable contributions from B and N orbitals. Both bands are strongly localized on the defect core, with 78% and 88% of the total DOS deriving from the core-atom orbitals.

In conclusion, our calculations indicate that the relative stability of antiphase boundaries (APB) with armchair and zigzag chiralities in planar boron nitride (BN)

is determined by B and N chemical potential conditions (emulating the corresponding synthesis conditions). In an N-rich synthesis environment, a zigzag APB with pentagonal and octagonal rings in its N-rich core is the most stable structure in this material (among the models we considered), while for B-rich or intrinsic conditions a stoichiometric armchair APB with tetragons and octagons in its cores is the most stable. Such stability transition as a function of B and N chemical potentials is shown to arise from a competition between “wrong-bond” (homopolar B-B and N-N bonds) and elastic-energy costs at the core of the APBs. This is contrasted with analogous cases of extended defects in graphene, where the geometry with pentagonal and octagonal rings is the most stable. In the presence of carbon dopants, a carbon-doped zigzag APB becomes the most stable boundary for the last third part of the interval of realistic B and N chemical potentials values, comprising the last part of the intrinsic region plus the N-rich region. The electronic structure of the APBs in monolayer BN is shown to be particularly distinct, with the pentagonal-octagonal APB depicting a defect-like electronic structure with deep bands in the band gap, and the tetragonal-octagonal APB depicting bulk-like shallow electronic bands derived from the corresponding band edges.

Note added: A brief account of the present work was previously presented in a scientific meeting, and a summary was published in Ref. 9. During the preparation of this manuscript, we became aware of a recent work²⁶ that also considers the A-APB in BN, of which we had no previous knowledge.

Acknowledgments

The authors acknowledge support from the Brazilian agencies CNPq, FAPEMIG, Rede de Pesquisa em Nanotubos de Carbono, INCT de Nanomateriais de Carbono, and Instituto do Milênio em Nanotecnologia-MCT.

* corresponding author; Electronic address: rw-nunes@fisica.ufmg.br

¹ A. H. Castro Neto, F. Guinea, N. M. R. Peres, K. S. Novoselov, and A. K. Geim, *Rev. Mod. Phys.* **81**, 109 (2009).

² F. Banhart, J. Kotakoski, and A. V. Krasheninnikov, *ACS Nano* **5**, 26 (2011).

³ M. U. Kahaly, S. P. Singh, and U. V. Waghmare, *Small* **4**, 2209 (2008).

⁴ J. Lahiri, Y. Lin, P. Bozkurt, I. I. Oleynik, and M. Batzill, *Nat. Nanotech.* **5**, 326 (2010).

⁵ S. S. Alexandre, A. D. Lúcio, A. H. C. Neto, and R. W. Nunes, *Nano Letters* **12**, 5097 (2012).

⁶ X. L. Li, X. J. Wu, X. C. Zeng, and J. L. Yang, *ACS Nano* **6**, 4104 (2012).

⁷ E. Machado-Charry, P. Boulanger, L. Genovese, N.

Mousseau, and P. Pochet, *Appl. Phys. Lett.* **101**, 132405 (2012).

⁸ W. Auwärter, M. Muntwiler, J. Osterwalder, and T. Greber, *Surf. Sci. Lett.* **545**, L735 (2003).

⁹ S. S. Alexandre, L. C. Gomes, H. Chacham, and R. W. Nunes, *Bulletin of the American Physical Society* **57**, <http://meetings.aps.org/link/BAPS.2012.MAR.B7.14> (2012).

¹⁰ J. Kotakoski, A. V. Krasheninnikov, U. Kaiser, and J. C. Meyer, *Phys. Rev. Lett.* **106**, 105505 (2011).

¹¹ W. Kohn and L. J. Sham, *Phys. Rev.* **140**, A1133 (1965).

¹² J. M. Soler, E. Artacho, J. D. Gale, A. Garcia, J. Junquera, P. Ordejon, and D. Sanchez-Portal, *J. Phys. Cond. Matt.* **14**, 2745 (2002).

¹³ J. P. Perdew, K. Burke, and M. Ernzerhof, *Phys. Rev. Lett.* **77**, 3865 (1996).

- ¹⁴ N. Troullier and J. L. Martins, Phys. Rev. B **43**, 1993 (1991).
- ¹⁵ R. M. Martin, Solid State Comm. **8**, 799 (1970).
- ¹⁶ W. Orellana and H. Chacham, Phys. Rev. B **63**, 63, 125205 (2001).
- ¹⁷ M. S. C. Mazzoni, R. W. Nunes, S. Azevedo, and H. Chacham, Phys. Rev. B **73**, 073108 (2006).
- ¹⁸ S. S. Alexandre, H. Chacham, and R. W. Nunes, Phys. Rev. B **63**, 045402 (2001).
- ¹⁹ S. S. Alexandre, R. W. Nunes, and H. Chacham, Phys. Rev. B **66**, 085406 (2002).
- ²⁰ S. Azevedo, M. S. C. Mazzoni, R. W. Nunes, and H. Chacham, Phys. Rev. B **70**, 205412 (2004).
- ²¹ Y. Liu, S. Bhowmick, and B. I. Yakobson, Nano Letters **11**, 3113 (2011).
- ²² K. K. Kim, A. Hsu, X. T. Jia, S. M. Kim, Y. S. Shi, M. Hofmann, D. Nezich, J. F. Rodriguez-Nieva, M. Dresselhaus, T. Palacios, and J. Kong, Nano Letters **12**, 161 (2012).
- ²³ C. H. Jin, F. Lin, K. Suenaga, and S. Iijima, Phys. Rev. Lett. **102**, 195505 (2009).
- ²⁴ J. C. Meyer, A. Chuvilin, G. Algara-Siller, J. Biskupek, and U. Kaiser, Nano Letters **9**, 2683 (2009).
- ²⁵ K. Kim, W. R. L. Lambrecht, and B. Segall Phys. Rev. B **53**, 16310 (1996).
- ²⁶ Y. Liu, X. Zou, and B. I. Yakobson ACS Nano **6**, 7053 (2012).